

A closest point method library for PDEs on surfaces with parallel domain decomposition solvers and preconditioners

Ian C.T. May^{1*}, Ronald D. Haynes² and Steven J. Ruuth³

^{1*}Department of Applied Mathematics, University of California
Santa Cruz, Santa Cruz, 95064, California, USA.

²Department of Mathematics, Memorial University of
Newfoundland, St. John's, A1C 5S7, Newfoundland, Canada.

³Department of Mathematics, Simon Fraser University, Burnaby,
V5A 1S6, British Columbia, Canada.

*Corresponding author(s). E-mail(s): imay1@ucsc.edu;

Contributing authors: rhaynes@mun.ca; sruuth@sfu.ca;

Abstract

The DD-CPM software library provides a set of tools for the discretization and solution of problems arising from the closest point method (CPM) for partial differential equations on surfaces. The solvers are built on top of the well-known PETSc framework, and are supplemented by custom domain decomposition (DD) preconditioners specific to the CPM. These solvers are fully compatible with distributed memory parallelism through MPI. This library is particularly well suited to the solution of elliptic and parabolic equations, including many reaction-diffusion equations. The software is detailed herein, and a number of sample problems and benchmarks are demonstrated. Finally, the parallel scalability is measured.

Keywords: Surface PDEs, reaction-diffusion equations, domain decomposition, parallel linear solvers

1 Introduction

The numerical solution of PDEs intrinsic to surfaces presents interesting challenges over their flat-space analogs. The closest point method (CPM) is an approach to discretize general surface-intrinsic PDEs over a wide class of surfaces. The software library presented here provides an MPI parallel implementation of the CPM built on top of PETSc [1]. This software is particularly well suited to solving surface intrinsic reaction-diffusion systems, generically of the form

$$\left(\frac{\partial}{\partial t} - \mu_i \Delta_{\mathcal{S}} \right) u_i = f_i(t, \mathbf{x}, \mathbf{u}), \quad (1)$$

where \mathbf{u} are the different species in the system, μ_i are the diffusion coefficients, and f_i are the nonlinear reaction terms coupling the systems together.

This software provides access to the extensive suite of tools within PETSc for use with the CPM, and additionally defines custom Schwarz-type domain decomposition solvers/preconditioners for equations of the form

$$(c - \Delta_{\mathcal{S}}) u = f, \quad (2)$$

where $c \in \mathbb{R}^+$ is a positive constant, and $\Delta_{\mathcal{S}}$ is the Laplace-Beltrami operator intrinsic to an embeddable surface $\mathcal{S} \subset \mathbb{R}^d$. These custom domain decomposition (DD) methods were first presented in [2], and subsequently expanded upon in [3]. Solving equation (1) semi-implicitly requires the solution of many elliptic systems. The provided custom DD preconditioners are well suited to these linear systems. Additionally, the flexibility of PETSc is maintained, and the use of other preconditioners within PETSc is trivial.

To date, most software for the CPM has been limited to the use of direct solvers on shared memory machines. The DD-CPM software detailed here provides the first known implementation of this method that can leverage larger distributed memory machines. This facilitates the application of the CPM to larger and more complicated problems. For elliptic PDEs, the dependence on direct solvers that has been present in most CPM implementations has also been lifted through the introduction of custom DD preconditioned Krylov methods compatible with the CPM. For reaction-diffusion equations, this software allows the use of fine grids to reliably capture either complex surface geometry and/or sharp features in the generated solutions. Indeed, the software has been kept general to allow many other equations to be posed and solved.

1.1 Existing software

There is little existing software for the CPM. An important resource is the `cp_matrices` repository [4], hosted by Prof. Colin Macdonald (coauthor of references [5–10]). This repository consists of MatLab and Python codes, and is mostly restricted to serial execution. For problems outside our framework, we suggest to start with the `cp_matrices` repository.

A large motivator for developing CPM specific DD methods was the experience that algebraic preconditioners did not perform well in all cases, and required a great deal of problem specific tuning. However, there may be cases where the built-in PETSc preconditioners perform well with little cost per iteration [11]. The back-end preconditioners and solvers used with the DD-CPM library can be substituted with PETSc options easily, and without re-compiling the library. An important goal of the development of this software is to maintain a high degree of flexibility and interoperability with other software packages.

2 Review of core methods

Before discussing the software, we will briefly review the closest point method (CPM), and the (optimized) restricted additive Schwarz (ORAS) domain decomposition method. To keep these reviews concrete and simple they will be constrained to equation (2); the consideration of more complicated equations will be deferred to Section 3.1.

2.1 Closest point method

Methods for the numerical solution of surface intrinsic PDEs generally take one of two approaches: discretize the surface itself, or find a solution in a higher dimensional embedding space. Surface parametrization methods [12] are very efficient and allow the use of familiar discretizations, but are limited to simple surfaces where the parametrization is known. With these methods the user may need to contend with coordinate singularities. Finite element methods acting on a triangulation of the surface [13] yield sparse symmetric systems for model equation (2), but are sensitive to the quality of the triangulation. Level set methods [14] embed the surface in a higher dimensional flat space, treating the surface implicitly, however the requisite artificial boundary conditions on the computational domain and the treatment of open surfaces are non-trivial.

The CPM [5, 15] is an embedding method that uses an implicit representation of the surface similar to the level set method. When implemented, the CPM is posed only over a small region of the embedding space, \mathbb{R}^d , near the surface. This dramatically reduces the number of unknowns in the discretization. The CPM has been applied to triangulated surfaces [9], surfaces of mixed codimension [15], moving surfaces [16], and even point cloud domains [7]. The DD-CPM library supports triangulated surfaces directly. Surfaces of mixed codimension and point cloud domains are both supported by allowing user defined closest point functions to be used. This software does not currently support moving surfaces.

In this section, the CPM is described for equation (2) over a simple closed surface to keep the presentation brief. The CPM utilizes familiar Cartesian discretizations of differential operators for surface PDEs by first extending the solution off the surface to a narrow tube in the embedding space. The extended solution is formed to be constant in the surface normal direction,

and is obtained through the closest point function

$$\begin{aligned} cp_S: \mathbb{R}^d &\rightarrow \mathcal{S} \\ \mathbf{x} &\mapsto \arg \min_{\mathbf{y} \in \mathcal{S}} \|\mathbf{x} - \mathbf{y}\|_2, \end{aligned} \quad (3)$$

which maps each point in the embedding space, $\mathbf{x} \in \mathbb{R}^d$, to the closest point on the surface. The extension operator E is defined as the composition of a function $f: \mathcal{S} \rightarrow \mathbb{R}$ with cp_S over the embedding space, i.e., $(Ef)(\mathbf{x}) := f(cp_S(\mathbf{x}))$ for $\mathbf{x} \in \mathbb{R}^d$. Importantly, the restriction of the Laplacian of an extended function, ΔEf , to the surface \mathcal{S} , is equivalent to the Laplace-Beltrami operator acting on that surface bound function, $\Delta_S f$ [5, 8, 15]. The core idea of the CPM lies in discretizing ΔE over an appropriate domain in the embedding space instead of discretizing Δ_S over the surface directly.

A structured grid with spacing h is placed over the embedding space, and points near the surface are collected into the set of active nodes Σ_A . The points neighboring the members of Σ_A are gathered into the set of ghost nodes Σ_G . The closest point function (3) is continuous on a region of \mathbb{R}^d that lies within a distance κ_∞^{-1} of the surface, where κ_∞ is an upper bound on the curvatures of \mathcal{S} [17]. The extent of the active nodes in Σ_A will be determined by the extension operator, defined next, and it is assumed that h is chosen small enough that all nodes in Σ_A and Σ_G lie within a distance κ_∞^{-1} of the surface. The active and ghost nodes for a circle embedded in \mathbb{R}^2 can be seen in the left panel of Figure 1.

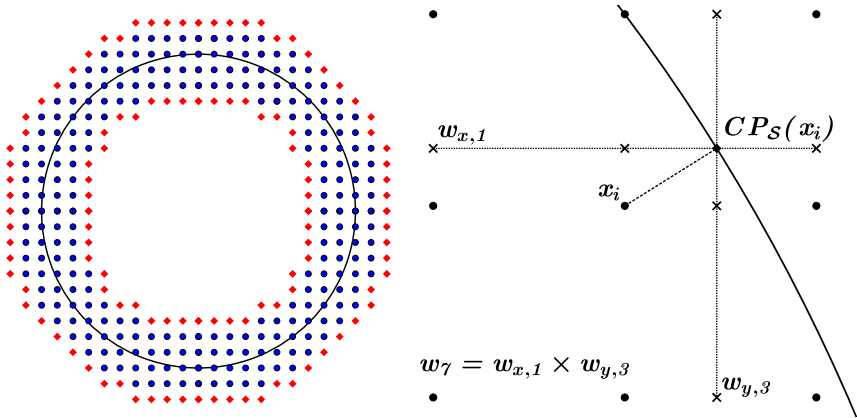


Fig. 1 The left panel shows the active nodes Σ_A (blue circles) and ghost nodes Σ_G (red diamonds) for a circle embedded in \mathbb{R}^2 . The right panel shows a bi-quadratic extension stencil for the node marked x_i . The values at all nine active nodes contribute to the value interpolated to $cp_S(x_i)$, and thus the extension back to x_i .

Given a function \tilde{f} sampled on Σ_A , the discrete extension operator \mathbf{E} produces a function \underline{f} on Σ_A that is constant in the surface normal direction and coincides with \tilde{f} on the surface. However, for $\mathbf{x}_i \in \Sigma_A$ the closest point $cp_S(\mathbf{x}_i)$

will generally not be another grid point. The function value $\tilde{f}(cp_S(\mathbf{x}_i))$ is therefore found by interpolating \tilde{f} over the points in Σ_A near $cp_S(\mathbf{x}_i)$. We use tensor product barycentric Lagrange interpolation [18] of degree p , and thus Σ_A contains the union of all $(p+1)^d$ cubes of grid points needed to perform this extension. The interpolation weights are independent of the data being interpolated, and \mathbf{E} can be written as a matrix where each row holds the interpolation weights for a given node in the computational domain (consisting of Σ_A and Σ_G). An example extension stencil can be seen in the right panel of Figure 1.

The ambient Laplacian, Δ , over the embedding space is discretized by standard second-order centered finite differences, denoted Δ^h . Along the edges of the tube of active nodes in Σ_A there will be incomplete finite difference stencils. The ghost nodes in Σ_G complete these stencils.

Finally, the discrete form of Δ_S will be given as the composition of Δ^h and \mathbf{E} . To apply the approach to implicit time stepping of diffusive problems [5], and eigenvalue problems [6], we use a stabilized discretization given by

$$\Delta_S^h = -\frac{2d}{h^2}\mathbf{I} + \left(\Delta^h + \frac{2d}{h^2}\mathbf{I}\right)\mathbf{E}, \quad (4)$$

where the removal of the diagonal elements from Δ^h avoids redundant self-interpolation.

2.2 Domain decomposition

Iterative methods for the solution of large linear systems are attractive for many reasons. Critical to this work, they may have greatly reduced time and memory requirements over direct solvers, and they are easy to parallelize on distributed memory machines. Domain decomposition (DD) methods seek to replace the solution of one large problem with the repeated solution of several smaller problems, and are particularly well suited to elliptic PDEs [19, 20]. These methods can be used as iterative solvers on their own, or embedded within a Krylov solver as a preconditioner [19]. The DD-CPM library implements Restricted Additive Schwarz (RAS) and Optimized Restricted Additive Schwarz (ORAS) solvers and preconditioners that respect the unique needs of the CPM.

For the CPM it will be beneficial to write the continuous formulation of the (O)RAS methods with respect to the surface intrinsic PDE (2). Consider splitting the global domain \mathcal{S} into N_S disjoint subdomains $\tilde{\mathcal{S}}_j$. Each disjoint subdomain is then grown to form an overlapping set of subdomains \mathcal{S}_j . The boundary of each subdomain, $\partial\mathcal{S}_j$, is split into parts lying in the nearby disjoint subdomains denoted as $\Gamma_{jk} \equiv \partial\mathcal{S}_j \cap \tilde{\mathcal{S}}_k$. Given an initial guess for the global solution $u^{(0)}$, defined at least on the artificial boundaries Γ_{jk} , we may solve

the local problems

$$\begin{cases} (c - \Delta_{\mathcal{S}}) u_j = f, & \text{in } \mathcal{S}_j, \\ \mathcal{T}_{jk} u_j = \mathcal{T}_{jk} u^{(n)}, & \text{on } \Gamma_{jk}, \forall k. \end{cases} \quad (5)$$

After the local solutions u_j are found on each overlapping subdomain, a new global solution may be formed with respect to the disjoint subdomains as

$$u^{(n+1)} = \sum_j u_j|_{\tilde{\mathcal{S}}_j}. \quad (6)$$

Then, with an updated solution on the artificial boundaries, the local problems may be solved again. The iteration then continues. The boundary operators \mathcal{T}_{jk} transmit data between the local problems and are thus referred to as *transmission operators*. The DD-CPM software considers transmission operators in one of two forms:

$$\mathcal{T}_{jk} = \text{identity}, \quad (7)$$

$$\mathcal{T}_{jk} = \left(\frac{\partial}{\partial \hat{\mathbf{q}}_{jk}} + \alpha \right), \quad (8)$$

where $\hat{\mathbf{q}}_{jk}$ is the unit conormal vector along Γ_{jk} . The first option enforces Dirichlet conditions on the local problems, while the second enforces Robin conditions. The Robin conditions also provide a parameter α which may be tuned to accelerate convergence.

ORAS solvers and preconditioners are constructed by discretizing equation (5) via the CPM. Finding discretizations of the transmission operators \mathcal{T}_{jk} , such that the DD iteration converges to the discrete single domain solution, requires care. A full discussion of the requisite considerations, and guidance on setting the parameter α , can be found in [2, 3].

3 Overview of the DD-CPM Software

The DD-CPM software is hosted as a public git repository on BitBucket. Users may obtain the current stable version from the release branch by calling:

```
git clone -b release \
https://mayianm@bitbucket.org/mayianm/DD-CPM.git DD-CPM
```

Similarly, one can obtain the software as it existed at the time of publication by cloning as above, and then calling:

```
git checkout NumAlgoVersion
```

Detailed installation instructions can be found in the `README.md` file present in the top level of the repository.

3.1 Specifying your own equations

Considering the `DDCPGrayScott` example, the essential ingredients in the driver code can be identified. A `ProblemDefinition` object, defined and setup on lines 62 – 71, holds all of the settings relevant to the setup of all other objects. An object of the `CPPPostProc` class (line 73) writes out all data files produced by the solver. The `GridFunc` and `DiffEq` objects created on lines 77 – 82 define the equation being solved. The usage of these classes is discussed in more detail below. The `CPMeshGlobal` class (used on line 84) defines the global computational domain and internally manages the partitioning of this domain into subdomains for the DD solvers to use. The `ProblemGlobal` object on line 86 builds the global system defined by the `DiffEq` object over the domain specified by the `CPMeshGlobal` object, and if DD solvers are desired, will also build the subproblems and manage communication internally. Finally, calling either the `solveTransient` method (line 91), or the `solveStationary` method (shown in the `DDCPPoisson` example) on the global problem will solve the defined equations.

3.1.1 Differential equations

The class `DiffEq` provides a container that combines one or more `GridFunc` objects, corresponding to the involved differential operators, with any forcing functions making up the total differential equation to be solved. For equations without time dependence, the assumed structure is $\mathcal{L}u = f(x)$ where \mathcal{L} is a differential operator expressed as a `GridFunc` object (discussed subsequently), and $f(x)$ is a forcing function dependent on the spatial variable. For instance line 84 in the `DDCPPoisson` example is:

```
DiffEq equation(pd,&shiftLap,&forcingFunc);
```

which encodes equation (2) by applying the grid function `shiftLap` to the left side of the equation, and filling the forcing term from `forcingFunc` defined at the top of the driver file.

For time dependent equations the assumed structure is $(\partial/\partial t + \mathcal{L})u = f(x, t, u)$, where \mathcal{L} is a spatial differential operator represented by a `GridFunc` object, and f is the forcing function which can now depend on the solution u and the time t in addition to spatial variable x . Lines 58 and 59 in the `DDCPHeat` example are:

```
GridFunc laplacian("LaplacianSecondOrder",
                  pd.mesh.dim,pd.mesh.delta,-1.0);
DiffEq equation(pd,&laplacian,&icHeat,&rhsHeat);
```

where `laplacian` is a `GridFunc` object encoding the (negative) Laplace-Beltrami operator. Note now that in addition to the spatial operator and the grid function, the `DiffEq` object now requires a function specifying the initial condition.

Finally, a `std::vector` of grid functions can also be supplied to specify multicomponent equations. Consider lines 89 – 92 in the `DDCPGrayScott` example:

```
GridFunc lapU("LaplacianSecondOrder",
              pd.mesh.dim, pd.mesh.delta, -gsPar_Du);
GridFunc lapV("LaplacianSecondOrder",
              pd.mesh.dim, pd.mesh.delta, -gsPar_Dv);
std::vector<GridFunc*> grayScottOp {&lapU, &lapV};
DiffEq equation(pd, grayScottOp, icGrayScott, rhsGrayScott);
```

where the two separate Laplace-Beltrami operators are weighted by the different diffusivities of the u and v components in the Gray-Scott equations. These four lines, along with reaction terms and initial conditions, fully encode equation (1).

3.1.2 Grid functions

The class `GridFunc` provides the user with a way to define their own operators without needing the specific details of the computational domain or the distributed matrix that the operator will eventually be represented by. In a two dimensional embedding space, the discrete Laplace-Beltrami operator shown in equation (4) can be obtained from the semidiscrete form

$$\begin{aligned} \Delta_S^h u(x, y) = & -\frac{4}{h^2} u(x, y) + \\ & \frac{1}{h^2} [u(cp_S(x+h, y)) + u(cp_S(x-h, y)) + \\ & u(cp_S(x, y+h)) + u(cp_S(x, y-h))] . \end{aligned} \quad (9)$$

Grid functions such as this are specified by three pieces of information: the stencil of nodes needed, the weight of each node in the stencil, and whether a node should be extended from the surface or not. The stencils for the extension operator are held internally, so this final item is simply a vector of booleans, and the full stencil including all nodes needed only for extension does not need to be specified.

Basic objects of the `GridFunc` class are formed from three `std::vector` objects holding these pieces of information. For ease, there are built-in grid functions for the identity, second-order accurate Laplace-Beltrami, and fourth-order accurate Laplace-Beltrami operators. Additionally, `GridFunc` objects can be added and composed to yield more complicated grid functions. For instance, the shifted Poisson equation (2) is written in the `DDCPPoisson` example as:

```
GridFunc laplacian("LaplacianSecondOrder",
                  pd.mesh.dim, pd.mesh.delta, 1.0);
GridFunc shift("Identity",
               pd.mesh.dim, pd.mesh.delta, 1.0);
GridFunc shiftLap = shift - laplacian;
```

where the final line encodes the total left-hand side operator. The biharmonic operator can be written as:

```
GridFunc laplacian (" LaplacianSecondOrder" ,
                    pd.mesh.dim,pd.mesh.delta ,1.0);
GridFunc biharmonic = laplacian*laplacian;
```

which is much simpler than writing the entire biharmonic stencil. Crucially, building these grid functions avoids doing significantly more expensive operations on large distributed matrices after their assembly.

4 Running the software

The DD-CPM software acts primarily as a library. Each equation to be solved is specified in a brief driver code which calls the DD-CPM library. A number of sample driver programs are included to demonstrate how to interact with the library, and how to solve a few representative equations. A small plotting script is included in the `python` directory nested under the DD-CPM root directory. The relevant plotting command to visualize the solution from each example is given. The DD-CPM library and sample driver programs generate output both to the terminal and in the form of HDF5 data files. The interpretation and use of these outputs is discussed. With all of the sample driver programs as reference, the section is concluded with a guide towards specifying user defined equations.

4.1 Included examples

The DD-CPM library comes with several example programs to demonstrate usage of the library and the structure of typical driver codes. The example programs do not rely on any particular choice of surface or level of parallelism. The example programs are

- **DDCPoisson.ex**: Solves the shifted Poisson equation, demonstrating stationary solvers and Laplace-Beltrami operators.
- **DDCPBiharmonic.ex**: Solves the shifted biharmonic equation, demonstrating stationary solvers and composition of operators.
- **DDCPHeat.ex**: Solves the heat equation, demonstrating implicit time stepping.
- **DDCPFitzhughNagumo.ex**: Solves the Fitzhugh-Nagumo equation, demonstrating implicit/explicit time stepping and multi-component equations.
- **DDCPGrayScott.ex**: Solves the Gray-Scott equation.
- **DDCPSchnackenberg.ex**: Solves the Schnackenberg equation, and includes a user defined surface.

After compilation, the binaries for these examples can be found in the `bin` directory, and the example source codes can be found in the `examples` directory.

Running each of the example programs follows essentially the same format:

```
mpiexec -n <nprocs> bin/DDCPEExample.ex \
-infile <path/to/inputfile> -cp_pc_ras
```

where `DDCPEExample` is replaced by one of the above example programs, `<nprocs>` is replaced by the number of processes you want to use for the run, and `<path/to/inputfile>` is the path to a file defining a surface and various default values. Many options can also be set on the command line to override values supplied by the input file. A full list of the available options can be obtained by running the example with the flag `-help`. The `-help` flag also gives several sample calls, specific to each example, with interesting options set to familiarize the user.

For examples using the included preconditioners (via flag `-cp_pc_ras`), it is required that the number of subdomains be divisible by the number of processes used. In most of the following examples we have specified 4 processes as most modern laptop and desktop computers can accommodate 4 threads. This may be changed depending on the resources available on your system. The subdomain count can easily be changed in all examples (via flag `-mesh_nparts <n>`) keeping in mind that the number of subdomains must be divisible by the number of processes used.

There is also a small plotting tool included in the `DD-CPM/python` directory. In the following examples, one call to the solver is shown alongside a command to generate a plot of the solution. All of the following commands are issued from inside the `DD-CPM/build` directory.

4.1.1 DDCPPoisson

The shifted Poisson equation, equation (2) above, can be solved on the circle with 2 processes and our ORAS preconditioner with 12 subdomains via:

```
mpiexec -n 2 bin/DDCPPoisson.ex \
-infile inputFiles/circle.icpm -cp_pc_ras \
-mesh_res 200 -mesh_nparts 12 -mesh_nover 4 \
-dd_trans_robfo -dd_osm_alpha 4 \
-ksp_converged_reason
```

where the argument `-cp_pc_ras` enables the custom DD-CPM preconditioner, `-mesh_res 200` sets the grid resolution to $h = 1/200$, `-mesh_nparts 12` sets the preconditioner to use $N_S = 12$ subdomains with an overlap width of $N_O = 4$ nodes on either side of where disjoint subdomains meet, and `-dd_trans_robfo -dd_osm_alpha 4` sets the preconditioner to use Robin transmission conditions with a weight of $\alpha = 4$ (consult equation (8)). The final argument `-ksp_converged_reason` tells PETSc to report the reason that the linear solver declared convergence.

The solution generated by this call can be visualized by:

```
python ../python/cpmpplot.py \
data/Circle200_3_12_4/Circle200_3_12_4ORAS000000.h5 \
cloud sol
```

which uses the included plotting tool to show the solution over the CPM point cloud. Alternatively, the forcing function can be visualized by calling:

```
python ../python/cpmplot.py \
data/Circle200_3_12_4/Circle200_3_12_4ORAS000000.h5 \
cloud rhs
```

4.1.2 DDCPBiharmonic

This example solves the shifted biharmonic equation

$$(c + \Delta_S^2) u = f(\mathbf{x}), \quad (10)$$

where, as before, c is a positive constant. The forcing function is given in spherical coordinates as

$$f(\theta, \phi) = 5000 \left(\theta^2 - \frac{\pi}{2} \theta \right) \cos(7\phi), \quad (11)$$

where here, and for any uses of spherical coordinates in the remainder, $\phi \in [0, 2\pi]$ is the azimuthal coordinate and $\theta \in [0, \pi]$ is the polar coordinate.

Note that the included domain decomposition preconditioners do not support biharmonic equations. Instead, one can either use preconditioners included in PETSc, or use a parallel direct solver. We take the latter approach here. Equation (10) can be solved on a sphere with 4 processes and the MUMPS [21, 22] parallel sparse direct solver by calling:

```
mpiexec -n 4 bin/DDCPBiharmonic.ex \
-infile inputFiles/sphere.icpm \
-mesh_res 20 -mesh_nparts 1 -ksp_type preonly \
-pc_type lu -pc_factor_mat_solver_type mumps
```

where the flags `-mesh_res 20` and `-mesh_nparts 1` set a grid spacing of $1/20$ and inform the library that no mesh partitioning is necessary. The remaining flags are all standard PETSc options to enable the MUMPS solver.

The grid function defining this operator can be obtained directly from the operator for the Laplacian by composition. Crucially, this is done before the global operator is constructed to avoid expensive matrix-matrix multiplication. This composition is quite simple, and is discussed in more detail in Section 3.1.2.

The solution can be visualized on the CPM point cloud by calling the included plotting tool as:

```
python ../python/cpmplot.py \
data/Sphere20_2_1_4/Sphere20_2_1_4RAS000000.h5 \
cloud sol
```

or over the surface itself by:

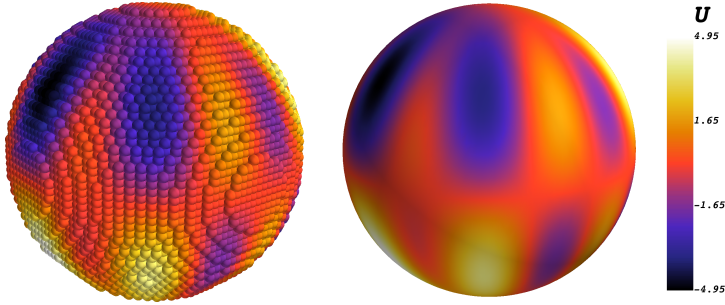


Fig. 2 The left and right panels show the solution of the shifted biharmonic equation (10) on the point cloud and polling surface respectively. The grid spacing is $h = 1/20$, and the forcing function is given in equation (11).

```
python ../python/cpmpplot.py \
data/Sphere20_2_1_4/Sphere20_2_1_4RAS000000.h5 \
poll sol
```

where `poll` indicates that the solution should be displayed on the the *polling surface* discussed in more detail below. The solution can be seen in Figure 2.

4.1.3 DDCPHeat

This example solves the heat equation

$$\frac{\partial u}{\partial t} - \Delta_{\mathcal{S}} u = f(\mathbf{x}, t), \quad (12)$$

where the time-dependent forcing function is given in spherical coordinates as

$$f(\theta, \phi, t) = \cos(t) \sin(3\phi). \quad (13)$$

The initial condition is $u(\mathbf{x}, 0) = 0$.

This can be solved on a sphere using 4 processes and our ORAS preconditioner over 12 subdomains by calling:

```
mpiexec -n 4 bin/DDCPHeat.ex \
-infile inputFiles/sphere.icpm -cp_pc_ras \
-mesh_res 20 -mesh_nparts 12 -mesh_nover 4 \
-dd_trans_robfo -dd_osm_alpha 4 \
-dd_osm_alpha_cross 40 \
-time_final 0.2 -ts_monitor -sub_pc_type ilu
```

The default time integrator is the PETSc TSARKIMEX method, and the linear systems that arise are solved with GMRES supplemented by a 12 subdomain DD-CPM ORAS preconditioner as seen by the flags `-cp_pc_ras -dd_trans_robfo -mesh_nparts 12`. The flags `-dd_osm_alpha 4 -dd_osm_alpha_cross 40` set the Robin weights, α in equation (8), to values of 4 and 40 along the interfaces and at cross-points respectively. The flag

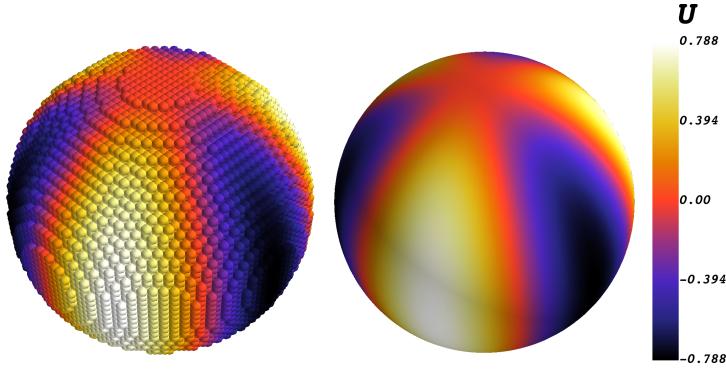


Fig. 3 The left and right panels show the solution of the heat equation (12) on the point cloud and polling surface respectively. The grid spacing is $h = 1/20$, the final time is $t = 0.2$, and the forcing function is given in equation (13).

`-sub_pc_type ilu` indicates to PETSc that the matrices defining the local problems are inverted using an incomplete LU factorization. This is generally useful for transient problems. The present flags set a final time of $T = 3500$.

The solution can be visualized on the CPM point cloud by calling the included plotting tool as:

```
python ../python/cpmplot.py \
data/Sphere20_2_12_4/Sphere20_2_12_4ORAS000006.h5 \
cloud sol
```

or over the polling surface by:

```
python ../python/cpmplot.py \
data/Sphere20_2_12_4/Sphere20_2_12_4ORAS000006.h5 \
poll sol
```

both of which can be seen in Figure 3.

4.1.4 DDCPFitzhughNagumo

This example solves the Fitzhugh-Nagumo equations

$$\begin{cases} \frac{\partial u}{\partial t} - D_u \Delta_S u = (0.1 - u)(u - 1)u - v, \\ \frac{\partial v}{\partial t} - D_v \Delta_S v = 0.01(0.5u - v) \end{cases} \quad (14)$$

where the diffusivities of each species are set as $D_u = 10^{-4}$ and $D_v = 10^{-7}$. The initial condition is chosen to be

$$u(\mathbf{x}, 0) = \begin{cases} 1, & x > 0, y > 0, z > 0 \\ 0, & \text{otherwise} \end{cases} \quad (15)$$

$$v(\mathbf{x}, 0) = \begin{cases} 1, & x > 0, y < 0, z > 0 \\ 0, & \text{otherwise} \end{cases}. \quad (16)$$

Time dependent problems require more setup, though most of the flags are self explanatory. This can be solved on a triangulated surface using 12 processes and the PETSc built-in block Jacobi preconditioner:

```
mpirun -n 12 bin/DDCPFitzhughNagumo.ex \
-infile inputFiles/triang.icpm \
-mesh_res 40 -mesh_nparts 12 -ksp_converged_reason \
-time_final 250 -ts_monitor
```

The triangulated surface is supplied in the form of a PLY file which is specified in the `triang.icpm` input file. The default option is the Stanford Bunny [23], though several other PLY files are included in the `DD-CPM/plyFiles` directory. The flag `-mesh_nparts 12` indicates the surface should be partitioned into 24 subdomains. Even though these subdomains are not utilized by the PETSc built-in preconditioners, this induces a beneficial ordering of the nodes. As such, even solves that do not utilize the custom DD preconditioners may take advantage of their existence.

The u component of the solution can be visualized by calling:

```
python ../python/cpmplot.py \
data/Triangulated40_2-12-3/Triangulated40_2-12-3RAS000176.h5 \
poll sol 0
```

and similarly the v component of the solution can be visualized by calling:

```
python ../python/cpmplot.py \
data/Triangulated40_2-12-3/Triangulated40_2-12-3RAS000176.h5 \
poll sol 1
```

each of which can be seen in Figure 4. Note that the solution here is not shown on the point cloud, but rather on the surface itself. This is specified by the `poll` option. When the DD-CPM library produces output files it will try to project the solution back onto the surface for later visualization. This requires that some triangulation of the surface is known. Of course, this triangulation is *not* used to solve the equations, but is needed to produce these visualizations. The options controlling this behavior are discussed in the following example. The solution on the point cloud can be seen by replacing `poll` with `cloud` in the above plotting calls.

4.1.5 DDCPGrayScott

This example solves the Gray-Scott equations

$$\begin{cases} \frac{\partial u}{\partial t} - D_u \Delta_{\mathcal{S}} u = (1 - u)F - uv^2 \\ \frac{\partial v}{\partial t} - D_v \Delta_{\mathcal{S}} v = uv^2 - (F + K)v \end{cases} \quad (17)$$

where the diffusivities of each species are chosen as $D_u = 6 \times 10^{-5}$ and $D_v = 3 \times 10^{-5}$, the feed rate is set at $F = 0.03$, and the kill rate is given in spherical coordinates by the function

$$k(r, \theta, \phi) = 0.06 + 0.001 \cos(\phi) \quad (18)$$

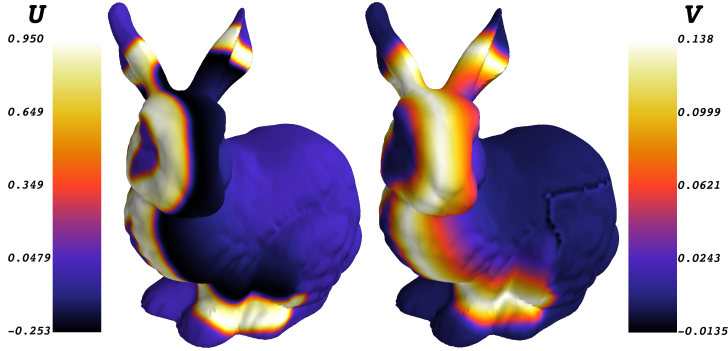


Fig. 4 The left and right panels show the u and v components of the solution to the Fitzhugh-Nagumo equation (14) at time $t = 250$. The initial conditions are set according to equation (16), and the grid spacing used is $h = 1/40$.

where ϕ is the azimuthal angle. The initial condition is chosen to be

$$u(r, \theta, \phi, 0) = 1 - e^{-5 \sin^2(5(\phi+0.5))} \quad (19)$$

$$v(r, \theta, \phi, 0) = e^{-5 \sin^2(5(\phi-0.5))}. \quad (20)$$

As in the previous example, the nonlinear coupling terms are advanced through time explicitly. To solve the Gray-Scott equation on a torus with 4 processes one could call:

```
mpirun -n 12 bin/DDCPGrayScott.ex \
-infile inputFiles/torus.icpm -cp_pc_ras \
-mesh_res 30 -mesh_nparts 12 -mesh_nover 2 \
-dd_trans_dirfo -time_final 10000 -pp_plotfreq 50 \
-pp_out_poll -mesh_npoll 400 -sub_pc_type ilu \
-ts_monitor
```

The diffusion terms are treated implicitly, and the linear systems that arise are solved with GMRES preconditioned by a 24 subdomain DD-CPM RAS preconditioner as seen by the flags `-cp_pc_ras` `-dd_trans_dirfo` `-mesh_nparts 24`. The flags `-sub_pc_type ilu` indicates to PETSc that the matrices defining the local problems are to be inverted using an incomplete LU factorization, which is generally useful for transient CPM problems. The time stepper defaults to using the PETSc TSARKIMEX3 method, and the present flags set a final time of $T = 30000$. Finally, the flags `-pp_plotfreq 50` `-pp_out_poll` `-mesh_npoll 400` inform the post-processor to write a data file every 50 time steps onto the polling surface only.

These solutions can be visualized by calling the included plotting tool as:

```
python ../python/cpmplot.py \
data/Torus30_2_12_2/Torus30_2_12_2RAS000418.h5 \
poll sol 0
```

and similarly the v component of the solution can be visualized by calling:

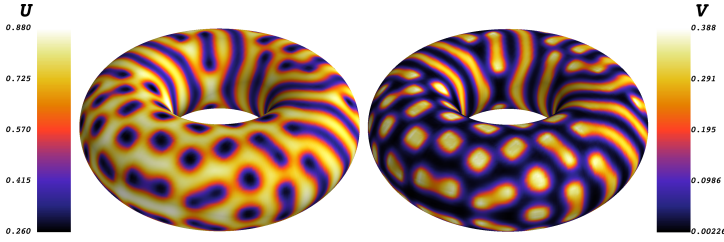


Fig. 5 The left and right panels show the u and v components of the solution to the Gray-Scott equation (17) at time $t = 30000$. The initial conditions and parameters are set according to equations (20) and (18), and the grid spacing used is $h = 1/40$.

```
python ../python/cpmplot.py \
data/Torus30_2_12_2/Torus30_2_12_2RAS000418.h5 \
poll sol 1
```

where in each call `poll` specifies that the polling surface should be used for visualization. The solutions can be seen in Figure 5. To see the solution on the CPM point cloud, one would need to replace `-pp_out_poll` by `-pp_out_all` in the above call to the solver, and replace `poll` by `cloud` in the visualization command.

4.1.6 DDCPSchnackenberg

The final example solves the Schnackenberg equations

$$\begin{cases} \frac{\partial u}{\partial t} - D_u \Delta_{\mathcal{S}} u = \delta_1 - u + u^2 v + \lambda v, \\ \frac{\partial v}{\partial t} - D_v \Delta_{\mathcal{S}} v = \delta_2 - u^2 v - \lambda v \end{cases} \quad (21)$$

where the parameters are chosen to be $D_u = 0.001$, $D_v = 0.1$, $\delta_1 = 0.003$, $\delta_2 = 0.7$, and $\lambda = 0.06$ inspired in part by [24]. The initial conditions are set as

$$u = 0.02 + \mathcal{U} \sin(5x) \cos(3y), \quad (22)$$

$$v = 4 + \mathcal{V} \sin(5xy) \sin(5x^3y) \quad (23)$$

where $\mathcal{U} \sim \mathcal{N}(0, 0.01)$ and $\mathcal{V} \sim \mathcal{N}(0, 1)$ are normally distributed random values.

This example also demonstrates how to implement user defined surfaces. Inside the driver code `DDCPSchnackenberg.cpp` there are functions defining the closest point function, a distance function, and a surface normal function, which are all handed to the library. In this case these functions correspond to a unit hemisphere.

The boundary conditions along the circular boundary are mixed between homogeneous Neumann and homogeneous Dirichlet. Taking ϕ as the azimuthal angle, any point that maps to the boundary where $\sin(3\phi) < -0.5$ is mirrored to enforce second order accurate homogeneous Dirichlet boundary conditions. The remainder of the circular boundary utilizes the natural homogeneous

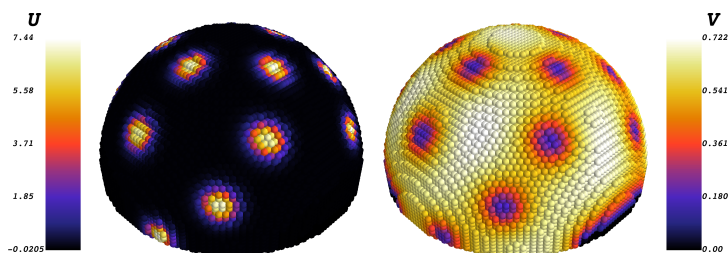


Fig. 6 The left and right panels show the u and v components of the solution to the Schnackenberg equation (21) at time $t = 50$. The initial conditions are given by equation (23), the grid spacing is $h = 1/30$, and the parameters used are $D_u = 0.001$, $D_v = 0.1$, $\delta_1 = 0.003$, $\delta_2 = 0.7$, and $\lambda = 0.06$.

Neumann boundary conditions. See [6] for details of the Dirichlet boundary formulation.

This equation can be solved on the user defined surface using 4 processes and our ORAS preconditioner over 12 subdomains by calling:

```
mpirun -n 12 bin/DDCPSchnackenberg.ex \
-infile inputFiles/user.icpm -cp-pc-ras -mesh-res 30 \
-mesh-nparts 12 -mesh-nover 4 -dd-trans-robfo \
-dd-osm-alpha 4 -dd-osm-alpha-cross 20 \
-time-final 100 -sub-pc-type ilu -ts-monitor \
-ts-adapt-dt-max 0.2
```

The u component of the solution can be visualized by calling:

```
python ../python/cpmpplot.py \
data/User20_2_12_4/User20_2_12_4ORAS000989.h5 \
cloud sol 0
```

and similarly the v component of the solution can be visualized by calling:

```
python ../python/cpmpplot.py \
data/User20_2_12_4/User20_2_12_4ORAS000989.h5 \
cloud sol 1
```

where each can be seen in Figure 6. Note that each of these calls visualize the solution over the point cloud. Currently there is no support for polling surfaces corresponding to user defined surfaces.

5 Profiling

The DD-CPM library yields great parallel scalability for moderate and large problems using hundreds of cores spread across a few nodes of a compute cluster. To demonstrate this scalability we focus on the shifted Poisson equation due to its ubiquity and relative simplicity. We remark before presenting the results that mesh partitioning currently relies on the serial version of METIS. This does present an early bottleneck when running large problems. However, this only occurs once in any run and does not pose any issue for problems

with up to a few million active grid points. All tests were performed on whole nodes of the Graham compute cluster managed by Compute Canada. Each node has two 16-core Intel E5-2683 v4 Broadwell 2.1 GHz processors and 125G of memory.

Each run is broken into three major phases: mesh construction and partitioning, global and local operator construction, and the GMRES solve. As discussed above, the meshing phase is not expected to scale due to the serial bottleneck there. The time required for each phase is recorded using the logging features of PETSc. Each test of scalability is performed using $N_P = 32, 64, 128$ processes, corresponding to 1, 2, and 4 full compute nodes on Graham respectively.

To assess the strong scalability, where a problem of fixed size is solved with progressively greater amounts of parallelism, we consider the torus described in Section 4.1.5 with a grid spacing of $h = \frac{1}{300}$ and tri-quadratic interpolation. This combination yields a problem with 4090560 unknowns. The linear system is solved with GMRES using the DD-CPM ORAS preconditioner with an overlap width of $N_O = 4$, and Robin weights $\alpha = 4$ and $\alpha^\times = 40$. All local problems inside the ORAS preconditioner are solved inexactly using an ILU factorization.

Phase	$N_P = 32, N_S = 32$	$N_P = 64, N_S = 64$	$N_P = 128, N_S = 128$
Meshing	42	43	44
Operator construction	53	32	18
GMRES	73	42	19
Total	169	115	82

Table 1 The time in seconds is shown for each phase in the solution of the shifted Poisson equation on a torus with $h = 300^{-1}$ and 4090560 unknowns. Here $N_S = N_P$ is fixed and excellent strong scalability is observed apart from the meshing phase.

The number of subdomains used must be divisible by the number of processes, giving two interesting options. First, Table 1 presents results from setting $N_S = N_P$. For $N_S = N_P = 32$ each disjoint subdomain contains approximately 128000 active nodes, and each overlapping subdomain contains approximately 140000 nodes. For $N_S = N_P = 64$ each disjoint subdomain contains approximately 64000 active nodes, and each overlapping subdomain contains approximately 73000 nodes. Finally, for $N_S = N_P = 64$ the disjoint and overlapping subdomains contain approximately 32000 and 38000 active nodes respectively. In this case the preconditioner is stronger for smaller process counts, but more expensive to apply due to the larger local problems. The operator construction and GMRES solve scale quite well, though the disparity in the size of the local problems is visible when comparing $N_P = 32$ to $N_P = 64$.

Alternatively, the number of subdomains can be fixed at $N_S = 128$ irrespective of the number of processes. This ensures that all of the local problems are the same size, and that the preconditioner being applied is the same in

Phase	$N_P = 32, N_S = 128$	$N_P = 64, N_S = 128$	$N_P = 128, N_S = 128$
Meshing	43	43	44
Operator construction	72	33	18
GMRES	77	49	19
Total	186	125	82

Table 2 The time in seconds is shown for each phase in the solution of the shifted Poisson equation on a torus with $h = 300^{-1}$ and 4090560 unknowns. Here $N_S = 128$ is fixed independent of the number of processes (compare to Table 1). Again, excellent strong scalability is observed apart from the meshing phase.

all cases. In this case, each disjoint subdomain contains approximately 32000 active nodes, and each overlapping subdomain contains approximately 38000 nodes. As shown in Table 2, the now weakened preconditioner (for the smaller process counts) leads to longer GMRES solution times. Similarly, for $N_P = 32$ and $N_P = 64$ each process is responsible for constructing and inverting multiple local operators.

Phase	$N_P = 32, N_S = 32$	$N_P = 64, N_S = 64$	$N_P = 128, N_S = 128$
Meshing	12	25	44
Operator construction	19	20	18
GMRES	10	16	19
Total	39	60	82

Table 3 The time in seconds is shown for each phase in the solution of the shifted Poisson equation on a torus on a sequence of finer meshes. Resolutions of $h = 160^{-1}$, $h = 230^{-1}$, and $h = 300^{-1}$, were used to keep the number of unknowns per process roughly constant. Excellent weak scalability is observed in the operator construction phase, while the time required in the solution phase slowly increases.

Weak scalability is assessed by fixing $N_S = N_P$, and varying the resolution of the problem such that the sizes of the disjoint partitions are roughly constant. For $N_S = N_P = 32$ the resolution is $h = \frac{1}{160}$ for a total of 1165840 unknowns with disjoint and overlapping subdomains of approximate size 37000 and 43000 respectively. For $N_S = N_P = 64$ the resolution is increased to $h = \frac{1}{230}$ for a total of 2406328 unknowns, and subdomains of approximately the same size. As can be seen in Table 3, the operator construction phase scales almost perfectly. The time required for the GMRES solution slowly climbs, which is to be expected since the included preconditioner incorporates only a single level.

6 Conclusion

The DD-CPM library provides a general purpose implementation of the closest point method with an emphasis on distributed memory parallelism. The DD-CPM library is particularly useful for surface intrinsic reaction-diffusion equations, where the included DD preconditioners can efficiently handle the

stiff diffusion terms implicitly. The DD-CPM library also handles domains in flat space with otherwise difficult boundaries, and with some development could be applied to coupled bulk-surface equations. The software could be similarly extended to handle fully implicit discretizations in time, with the given preconditioners aiding in the solution of the linear systems that arise inside the Newton iterations. Additionally, the DD-CPM library could make an effective back end for eigenvalue problems due to the interoperability of PETSc and SLEPc.

Declarations

Funding

The authors gratefully acknowledge the financial support of NSERC Canada (RGPIN 2016-04361 and RGPIN 2018-04881). This research was enabled in part by support provided by ACEnet (ace-net.ca) and Compute Canada (www.computecanada.ca).

References

- [1] Balay, S., Gropp, W.D., McInnes, L.C., Smith, B.F.: Efficient Management of Parallelism in Object-Oriented Numerical Software Libraries, pp. 163–202. Birkhäuser Boston, Boston, MA (1997). https://doi.org/10.1007/978-1-4612-1986-6_8
- [2] May, I.C.T., Haynes, R.D., Ruuth, S.J.: Domain decomposition for the closest point method. In: Domain Decomposition Methods in Science and Engineering XXV. Lecture Notes in Computational Science and Engineering ; 138, pp. 458–465. Springer, Cham (2020). International Conference on Domain Decomposition Methods in Science and Engineering (25th : 2018 : St. John’s, N.L.)
- [3] May, I.C.T., Haynes, R.D., Ruuth, S.J.: Schwarz solvers and preconditioners for the closest point method. *SIAM Journal on Scientific Computing* **42**(6), 3584–3609 (2020). <https://doi.org/10.1137/19M1288279>
- [4] Macdonald, C.B.: CP_Matrices. GitHub (2018). https://github.com/cbm755/cp_matrices
- [5] Macdonald, C.B., Ruuth, S.J.: The implicit closest point method for the numerical solution of partial differential equations on surfaces. *SIAM J. Sci. Comput.* **31**(6), 4330–4350 (2010)
- [6] Macdonald, C.B., Brandman, J., Ruuth, S.J.: Solving eigenvalue problems on curved surfaces using the closest point method. *J. Comput. Phys.* **230**(22), 7944–7956 (2011)

- [7] Macdonald, C.B., Merriman, B., Ruuth, S.J.: Simple computation of reaction–diffusion processes on point clouds. *Proceedings of the National Academy of Sciences* **110**(23), 9209–9214 (2013). <https://doi.org/10.1073/pnas.1221408110>
- [8] März, T., Macdonald, C.B.: Calculus on surfaces with general closest point functions. *SIAM J. Numer. Anal.* **50**(6), 3303–3328 (2012)
- [9] Macdonald, C.B., Ruuth, S.J.: Level set equations on surfaces via the closest point method. *Journal of Scientific Computing* **35**(2), 219–240 (2008)
- [10] Chen, Y., Macdonald, C.B.: The closest point method and multigrid solvers for elliptic equations on surfaces. *SIAM J. Sci. Comput.* **37**(1), 134–155 (2015)
- [11] May, D.A., Sanan, P., Rupp, K., Knepley, M.G., Smith, B.F.: Extreme-scale multigrid components within PETSc. In: *Proceedings of the Platform for Advanced Scientific Computing Conference. PASC ’16. Association for Computing Machinery, New York, NY, USA* (2016). <https://doi.org/10.1145/2929908.2929913>
- [12] Floater, M.S., Hormann, K.: *Surface Parameterization: a Tutorial and Survey*, pp. 157–186. Springer, Berlin, Heidelberg (2005)
- [13] Dziuk, G., Elliott, C.M.: Surface finite elements for parabolic equations. *Journal of Computational Mathematics* **25**(4), 385–407 (2007)
- [14] Bertalmio, M., Cheng, L.-T., Osher, S., Sapiro, G.: Variational problems and partial differential equations on implicit surfaces. *J. Comput. Phys.* **174**(2), 759–780 (2001)
- [15] Ruuth, S.J., Merriman, B.: A simple embedding method for solving partial differential equations on surfaces. *J. Comput. Phys.* **227**(3), 1943–1961 (2008)
- [16] Petras, A., Ruuth, S.J.: PDEs on moving surfaces via the closest point method and a modified grid based particle method. *J. Comput. Phys.* **312**, 139–156 (2016)
- [17] Chu, J., Tsai, R.: Volumetric variational principles for a class of partial differential equations defined on surfaces and curves. *Res. Math. Sci.* **5**(2), 19 (2018)
- [18] Berrut, J.-P., Trefethen, L.N.: Barycentric Lagrange interpolation. *SIAM Review* **46**(3), 501–517 (2004)

- [19] Dolean, V., Jolivet, P., Nataf, F.: An Introduction to Domain Decomposition Methods: Algorithms, Theory, and Parallel Implementation. SIAM, Philadelphia, PA, USA (2015)
- [20] Toselli, A., Widlund, O.: Domain Decomposition Methods—algorithms and Theory. Springer Series in Computational Mathematics, 34. Springer, Berlin ; New York (2005)
- [21] Amestoy, P.R., Duff, I.S., L’Excellent, J.-Y., Koster, J.: A fully asynchronous multifrontal solver using distributed dynamic scheduling. SIAM Journal on Matrix Analysis and Applications **23**(1), 15–41 (2001)
- [22] Amestoy, P.R., Guermouche, A., L’Excellent, J.-Y., Pralet, S.: Hybrid scheduling for the parallel solution of linear systems. Parallel Computing **32**(2), 136–156 (2006)
- [23] Turk, G., Levoy, M.: Zippered polygon meshes from range images. In: Proceedings of the 21st Annual Conference on Computer Graphics and Interactive Techniques. SIGGRAPH ’94, pp. 311–318. ACM, Orlando, Florida, United States of America (1994)
- [24] Noufaey, K.S.A.: Stability analysis for Selkov-Schnakenberg reaction-diffusion system. Open Mathematics **19**(1), 46–62 (2021). <https://doi.org/10.1515/math-2021-0008>